

RGD-Functionalized Melanin Nanoparticles for Intraoperative Photoacoustic Imaging-Guided Breast Cancer Surgery

Jing-Jing Liu

Xiamen University

Zun Wang

Shantou University Medical College

Li-Ming Nie

Xiamen University

Yuan-Yuan Zhu

Xiamen University

Ge Li

Xiamen University

Lin-Ling Lin

Xiamen University

Min Chen

Xiamen University

Guo-Jun Zhang (✉ guoj_zhang@yahoo.com)

Xiamen University <https://orcid.org/0000-0001-5182-5887>

Research Article

Keywords: melanin, bioimaging, photoacoustic imaging, breast cancer, tumour 59 detection, imaging-guided surgery

Posted Date: April 26th, 2021

DOI: <https://doi.org/10.21203/rs.3.rs-429256/v1>

License: © ⓘ This work is licensed under a Creative Commons Attribution 4.0 International License.

[Read Full License](#)

1 RGD-functionalized melanin nanoparticles for intraoperative
2 photoacoustic imaging-guided breast cancer surgery

3 Jing-Jing Liu^{1,2,#}, Zun Wang^{5,7#}, Li-Ming Nie^{6,8}, Yuan-Yuan Zhu^{1,2}, Ge Li^{1,2},
4 Lin-Ling Lin^{1,2}, Min Chen^{2,3,4,*} and Guo-Jun Zhang^{1,2,3,*}
5

6 ¹ Cancer Center & Department of Breast and Thyroid Surgery, Xiang'an Hospital
7 of Xiamen University, School of Medicine, Xiamen University, 2000 Xiang'an
8 Road East, Xiamen, 361101, Fujian, China.

9 ² Key Laboratory for Endocrine-Related Cancer Precision Medicine of Xiamen,
10 Xiang'an Hospital of Xiamen University, Xiamen, Fujian, China.

11 ³ Cancer Research Center, School of Medicine, Xiamen University, Xiamen,
12 China.

13 ⁴ Clinical Central Research Core, Xiang'an Hospital of Xiamen University, No.
14 2000, Xiang'an Road East, Xiamen, 361101, Fujian, China.

15 ⁵ ChangJiang Scholar's Laboratory, Shantou University Medical College, 515041,
16 Shantou, China.

17 ⁶ State Key Laboratory of Molecular Vaccinology and Molecular Diagnosis &
18 Center for Molecular Imaging and Translational Medicine, School of Public
19 Health, Xiamen University, Xiamen, 361102, China.

20

21 # These authors contributed equally to this work.

22

23 * **Corresponding authors:** Guojun Zhang, Phone: 0086-592-28899988, e-mail:
24 gjzhang@xah.xmu.edu.cn; Min Chen, Phone: 0086-0592-2889270, e-mail:
25 mchen@xah.xmu.edu.cn;
26

26

27 Note: Present Address:

28 ⁷ Department of Breast and Thyroid Surgery, Shenzhen Baoan Women's and
29 Children's Hospital, Jinan University, 518133, Shenzhen, China.

30 ⁸ Department of Radiology and Optical Imaging Laboratory, Guangdong
31 Provincial People's Hospital, Guangdong Academy of Medical Sciences, 510080,
32 Guangzhou, China.

33

34 **Abstract**

35 **Purpose:** Obtaining tumour-free margins is critical for avoiding re-excision and
36 reducing local recurrence following breast-conserving surgery (BCS); however, it
37 remains challenging. Imaging-guided surgery provides precise detection of residual
38 lesions and assists surgical resection. Herein, we describe water-soluble melanin
39 nanoparticles (MNPs) conjugated with cyclic Arg-Gly-Asp (cRGD) peptides for breast
40 cancer photoacoustic imaging (PAI) and surgery navigation.

41 **Methods:** cRGD-MNPs was synthesized and characterized for morphology,
42 photoacoustic characteristics and stability. Tumour targeting and toxicity were
43 determined by cells and tumour-bearing mice. PAI was used to locate the tumour and
44 guide surgical resection in MDA-MB-231 tumour-bearing mice.

45 **Results:** The cRGD-MNPs exhibited excellent tumour-targeting *in vitro* and *in vivo*,
46 with low toxicity. Intravenous administration of cRGD-MNPs to MDA-MB-231
47 tumour-bearing mice showed an approximately 2.1-fold enhancement in photoacoustic
48 (PA) intensity at 2 h, and the ratio of the PA intensity at the tumour site compared to
49 that in the surrounding normal tissue was 3.2 ± 0.1 , which was much higher than that
50 using MNPs alone (1.7 ± 0.3). Similarly, the PA signal in the mammary glands
51 containing spontaneous breast cancer was enhanced (2.5 ± 0.3 -fold) in MMTV-PyVT
52 transgenic murine model. Preoperative screening by PAI could assess tumour volume
53 and offer a three-dimensional (3D) reconstruction image for accurate surgical planning.
54 Surgical resection following real-time PAI on the tumour bed showed high consistency
55 with histopathological analysis.

56 **Conclusion:** These results highlight that cRGD-MNPs combined with PAI provide
57 a powerful tool for breast cancer imaging and precise tumour resection. cRGD-MNPs
58 with good PA properties have great potential for clinical translation.

59 **Keywords:** melanin, bioimaging, photoacoustic imaging, breast cancer, tumour
60 detection, imaging-guided surgery

61

62 **Introduction**

63 Nearly half of patients with early breast cancer undergo breast-conserving surgery
64 (BCS) with adjuvant radiation therapy [1]. BCS involves the removal of the primary
65 tumour with a margin of surrounding normal breast tissue. Although BCS is the
66 standard of care treatment for early breast cancer patients [2], a potential downside is
67 the failure to achieve clear or negative margins with lumpectomy. In particular, 20–40%
68 of patients require additional operative intervention by re-excision or even mastectomy
69 [3]. Re-excision surgery increases the risk of complications (e.g., infection and
70 unsatisfactory aesthetic results) and potentially postpones systemic treatment. It also
71 increases health care costs and burden and harms patients both physically and
72 psychologically.

73 During BCS, surgeons typically use visual inspection and tactile feedback to
74 determine the tumour location and set resection margins. However, it is difficult to
75 discriminate tumour margins from surrounding normal tissue macroscopically. Frozen
76 section and imprint cytology are applied clinically for intraoperative margin assessment.
77 These methods have the potential to lower the rates of positive margins, but they are
78 labour-intensive and time-consuming and have low sensitivity due to sampling rate
79 limitations [4, 5]. Currently, there have been multiple emerging intraoperative imaging
80 tools for real-time margin assessment, including wire-guided localization [6],
81 intraoperative ultrasound [7] and postoperative techniques (intraoperative specimen
82 mammography/micro-computed tomography) [8]. Due to their anatomical imaging
83 modalities and limited tumour specificity, these methods have not been widely used for
84 margin assessment. Fluorescence-guided surgical navigation is a high sensitivity
85 technique using the injection of a fluorescent contrast agent that is a promising
86 intraoperative tool for precise tumour resection [9]. However, this technique is
87 hampered by a limited penetration depth because of light scattering and signal
88 attenuation [10].

89 Recently, photoacoustic imaging (PAI) has been developed as a novel imaging
90 technology for biomedical applications. PAI detects optical absorption contrast
91 acoustically via the photoacoustic (PA) effect, a physical phenomenon that converts

92 absorbed optical energy into acoustic energy [11]. Based on endogenous contrast
93 molecules (e.g., oxyhaemoglobin, deoxyhaemoglobin, lipid, or DNA-RNA), PAI has
94 been used in the clinic trial to demonstrate its highly desirable capabilities for breast
95 cancer imaging *in vivo* and *ex vivo*, particularly for assessing tumour margins
96 macroscopically and microscopically [12-14]. However, intrinsic chromophores
97 provide access to only a limited range of biological processes but low tumour-imaging
98 contrast. Hence, molecular PAI for breast cancer still requires a targeted contrast agent
99 that can selectively bind to surface receptors on cancer cells or respond to the tumour
100 microenvironment [11, 15].

101 Natural melanin is a group of biopigments with multifunctionality (i.e., ultraviolet
102 protection, radical scavenging, and photothermal conversion) [16]. Due to its good
103 intrinsic biocompatibility, natural melanin or synthetic melanin-like nanomaterials have
104 been successfully developed as novel nano-bioplatforms in bioimaging, therapy,
105 theranostics, and biosensing [17, 18]. As an endogenous PA contrasting agent, melanin
106 was used to detect the metastatic status of *ex vivo* human melanoma sentinel lymph
107 nodes by multispectral optoacoustic imaging[19]. The results showed an excellent
108 correlation with the histological assessment of melanoma cell infiltration with 100%
109 sensitivity and 62% specificity [19].

110 In this study, we conducted a comprehensive study of the feasibility of the PAI
111 method for improving the detection and accurate removal of breast cancer using
112 targeted melanin nanoparticles (MNPs) conjugated with cyclic Arg-Gly-Asp (cRGD)
113 (Scheme 1). Our data support the potential clinical application of cRGD-MNPs as a
114 novel tumour-specific PA contrast agent for imaging-guided BCS.

115 **Materials and methods**

116 **Reagents**

117 Melanin was obtained from Sigma-Aldrich. Sodium hydroxide, hydrochloric acid
118 and NH₄OH solution (28 wt%) were purchased from Sinopharm Chemical Reagent Co.,
119 Ltd. Amine-PEG₅₀₀₀-amine (NH₂-PEG₅₀₀₀-NH₂, 5 kDa) was obtained from Shanghai
120 Aladdin Bio-Chem Technology Co., LTD. CellTiter 96 AQueous One Solution Cell
121 Proliferation Assay (MTS) was purchased from Promega, phosphate-buffered saline
122 (PBS) was purchased from Solarbio and c(RGDfC) was from GL Biochem. Melanin
123 staining kit was purchased from Servicebio. Dulbecco's modified eagle's medium
124 (DMEM), fetal bovine serum (FBS), and penicillin-streptomycin were purchased from
125 Gibco. Mammary Epithelial Cell Growth Medium (MEGM) BulletKit was purchased
126 from Lonza.

127 **Cell culture**

128 The human breast cancer cell line MDA-MB-231 and non-cancerous mammary
129 epithelial cell line MCF-10A were purchased from Procell Life Science & Technology
130 Co., Ltd. , and cells with passage number < 25 were used in the experiment. MDA-MB-
131 231 cells were cultured in DMEM supplemented with 10% FBS and 1% penicillin-
132 streptomycin. MCF-10A cells were cultured in MEGM supplemented with BPE, hEGF,
133 insulin, hydrocortisone, and GA-1000. The cells were grown as sub-confluent
134 monolayers at 37 °C under the water-saturated environment with 5% CO₂.

135 **Animals**

136 All animal experiments were performed in compliance with the Guidelines for the
137 Care and Use of Research Animals established by the Xiamen University Animal
138 Studies Committee. Female BALB/c nude mice and BALB/c mice (4–6 weeks,
139 approximately 20 g) were purchased from the Experimental Animal Center of Xiamen
140 University and kept under sterile conditions. FVB/N-Tg(MMTV-PyVT)634Mul/J
141 transgenic mice were purchased from the Jackson Laboratory and raised under specific-
142 pathogen-free conditions.

143 **Preparation of cRGD-MNPs**

144 The cRGD-MNPs were obtained as previously described [20]. Briefly, melanin (2
145 mg/mL) was dissolved in NaOH aqueous solution (0.1 N) followed by the rapid
146 addition of HCl aqueous solution (0.1 N) to a pH of 7.0 under sonication. The
147 neutralised solution was centrifuged and washed with deionized water several times.
148 The black solid of MNPs was obtained by freeze-drying. The MNPs aqueous solution
149 (1 mg/mL, pH = 9) was added dropwise into an NH₂-PEG₅₀₀₀-NH₂ aqueous solution.
150 After vigorous stirring for 12 h, the PEG-modified MNPs were retrieved by
151 centrifugation and washed several times to remove the unreacted NH₂-PEG₅₀₀₀-NH₂.
152 The PEGylated MNPs (1 mg/mL, pH = 7.2) were incubated with 4-(N-
153 maleimidomethyl)cyclohexane-1-carboxylic acid 3-sulfo-N-hydroxysuccinimide ester
154 sodium salt (sulfo-SMCC) solution (1.2 mg in 36 μ L of dimethyl sulfoxide) for 2 h at
155 room temperature. The complexes were purified using a PD-10 column. The c(RGDfC)
156 solution (120 μ L of 5 mM in degassed water) was added to the purified MNPs with
157 stirring for 24 h at 4°C. The excessive RGD peptide was removed using a PD-10
158 column. The final cRGD-MNPs were filtered through a 0.22 μ m filter.

159 **Characterisation of MNPs**

160 Transmission electron microscopy images were recorded using a Talos F200s
161 transmission electron microscope (FEI, USA) at an accelerating voltage of 100 kV. The
162 MNPs or cRGD-MNPs aqueous solution was dropped onto a carbon-coated copper grid
163 and air-dried. The ¹H NMR spectra were recorded at 20°C on a 400 MHz NMR
164 spectrometer (Bruker) using D₂O as the solvent. Zeta potentials were measured using a
165 laser particle size analyser system (Malvern, Zetasizer Nano ZS90). The absorption
166 spectra were obtained using a Multiskan Spectrum Microplate Spectrophotometer
167 (Thermo, USA).

168 **PAI system**

169 Both PA and US images were recorded using the Vevo LAZR-X photoacoustic
170 imaging system (VisualSonics, FujiFilm, Japan). A tunable laser (680–970 nm) with a

171 repetition rate of 20 Hz and a 256-element linear array with the main frequency of 40
172 MHz was used to obtain single-plane, full-spectrum and 3D PA images. The 3D
173 scanning was controlled using an electric motor with a step length of 0.14 mm. The
174 quantified PA signal intensities within the region of interest (ROI) of each image were
175 analysed using the Vevo LAB tool (VisualSonics, FujiFilm, Japan).

176 **PA signal of cRGD-MNPs**

177 For evaluating the PA performance of nanoparticles, MNPs and cRGD-MNPs (120
178 μM) were scanned for PAI at different wavelengths ranging from 680 to 970 nm
179 (interval = 5 nm) to detect the optimum excitation wavelength. Different concentrations
180 (3.75–120 μM) of MNPs and cRGD-MNPs were dispersed in PBS and triggered by the
181 optimal excitation wavelength to acquire the corresponding PA images. For
182 photostability analysis, PA images of the MNPs and cRGD-MNPs solutions (120 μM)
183 were obtained at different time points (0, 2, 4, 6 and 7 days) using a 680 nm excitation.

184 **Cellular uptake of cRGD-MNPs**

185 MDA-MB-231 cells (3×10^5 per well) were seeded in 6-well plates and cultured for
186 24 h. The old medium was replaced with medium containing 0.125 μM cRGD-MNPs.
187 After incubation for various times (1, 2, 4 or 8 h), the medium was removed, and the
188 cells were washed three times with PBS. The cells were harvested, fixed with 4%
189 paraformaldehyde solution for 20 min, resuspended in PBS and counted. The same
190 amount of cell suspension (20 μL) was placed in a microcentrifuge tube and then the
191 tube was fixed on the imaging table. PAI was performed on the MDA-MB-231 cell
192 samples at a wavelength of 680 nm using the Vevo LAZR-X system. For the
193 concentration gradient experiment, MDA-MB-231 cells were incubated in medium
194 containing the cRGD-MNPs (0.125, 0.25, 0.5 or 1 μM) for 4 h. The cells were collected
195 and imaged as above. To investigate the effect of RGD on MNPs uptake, MDA-MB-
196 231 cells were treated for 4 h with medium containing 0.5 μM MNPs, PEG-MNPs or
197 cRGD-MNPs and then subjected to PAI analysis. For the RGD blocking experiment,
198 MDA-MB-231 and MCF-10A cells were seeded in 6-well culture plates and incubated

199 with 0.5 μ M cRGD-MNPs for 4 h. For the $\alpha_v\beta_3$ integrin-blocking group, MDA-MB-
200 231 cells were co-incubated with free RGD (100 μ M). The samples were assessed by
201 PAI.

202 **Preparation of Rho-MNPs and Rho-cRGD-MNPs**

203 Rhodamine (30 μ L, 5 mg/mL) was added to the MNPs or cRGD-MNPs solutions (1
204 mL, 2 mg/mL). After stirring at room temperature for 1 h, the solution was transferred
205 to an ultrafiltration centrifuge tube (Millipore Amicon Ultra, 30 kDa) and centrifuged
206 several times (4000 rpm, 15 min) to remove the free or unstable rhodamine, yielding
207 the rhodamine-labelled MNPs (Rho-MNPs) and cRGD-MNPs (Rho-cRGD-MNP).

208 **Location of cRGD-MNPs by confocal microscopy**

209 MDA-MB-231 (1×10^5 cells) were seeded in confocal dishes and allowed to adhere
210 for 24 h. The Rho-cRGD-MNPs were added to the culture medium with or without free
211 RGD (100 μ M) at the times and concentrations described above. The cells were fixed
212 with 4% paraformaldehyde and counterstained with DAPI to visualise nuclei. The
213 fluorescence images of the cells were collected using a Nikon confocal laser scanning
214 microscope.

215 ***In vitro* cytotoxicity assay**

216 MNPs cytotoxicity was determined in MDA-MB-231 cells using the MTS assay.
217 MDA-MB-231 cells (5×10^3 /well) were incubated in 96-well plates for 24 h. Cells were
218 then cultured in medium supplemented with the different MNPs (0.625, 1.25, 5 and 10
219 μ M) for 72 h. After the incubation, MTS (10 μ L, 0.5 mg/mL) was added to each well,
220 and the cells were incubated for 2 h at 37°C. The absorbance was measured at 490 nm
221 using a microplate reader. The absorbance of the untreated cells was used as the
222 reference value for calculating 100% cell viability. Five replicates were conducted for
223 each group.

224 **MDA-MB-231 breast cancer xenograft mouse model**

225 MDA-MB-231 cells (1×10^6 in 100 μ L PBS) were inoculated subcutaneously in a

226 single flanks of nude mice. When tumour volume reached 100 mm^3 , the tumour-bearing
227 mice were subjected to *in vivo* PAI and biodistribution studies.

228 ***In vivo* tumour PAI in MDA-MB-231 tumour-bearing mice**

229 To determine the optimal concentration range of the MNPs, mice were randomly
230 allocated into groups and injected with different concentrations of RGD-PEG-MNPs
231 ($50 \mu\text{M}$, $100 \mu\text{M}$ or $200 \mu\text{M}$, $200 \mu\text{L}$) via the tail vein. PA images were collected at
232 different time points (pre, 1, 2, 4 or 12 h) using the Vevo LAZR-X at 680 nm, and the
233 average PA intensities in the tumour regions were measured. To detect the tumour
234 targeting capability of the cRGD-MNPs, MDA-MB-231 tumour-bearing mice were
235 randomly divided into MNPs and cRGD-MNPs groups ($n = 3$ per group). The mice
236 were intravenously injected with the MNPs or cRGD-MNPs ($100 \mu\text{M}$, $200 \mu\text{L}$),
237 respectively. PA images were collected, and the intensities measured.

238 **The biodistribution of MNPs and cRGD-MNPs in MDA-MB-231 tumour-bearing** 239 **mice**

240 To determine the biodistribution of the nanoprobes *in vivo*, MDA-MB-231 tumour-
241 bearing mice ($n = 3$ per group) were intravenously injected with Rho-MNPs or Rho-
242 cRGD-MNPs ($100 \mu\text{M}$, $200 \mu\text{L}$). The major organs and tumours of mice were harvested
243 2 h post-injection for *ex vivo* fluorescence imaging using the IVIS Lumina imaging
244 system (PerkinElmer, USA). The relative fluorescence intensities were measured.

245 **PAI and pathological analysis of spontaneous breast cancer in transgenic mice**

246 The FVB/N-Tg(MMTV-PyVT)634Mul/J transgenic mice model spontaneously
247 develops invasive breast cancer in each mammary gland between 6 and 12 weeks of
248 age. To further confirm the tumour targeting specificity of the cRGD-MNPs, mice with
249 breast cancer (age 6–8 weeks, $n = 6$) were intravenously injected with the cRGD-MNPs
250 ($100 \mu\text{M}$, $200 \mu\text{L}$). US and PA images were obtained before injection and 2 h post-
251 injection with excitation at 680 nm. In addition, the 4th and 5th mammary glands of the
252 transgenic mice (age 8 weeks, $n = 3$) with breast cancer were divided into four sections
253 (P1-4) for PAI *in vivo* and *in vitro* 2 h after nanoprobe injection. After imaging, the

254 mammary tissue was fixed with formalin and embedded in paraffin. Tissue sections (4
255 μm) were stained with haematoxylin and eosin (H&E), according to standard methods.

256 **Melanin staining**

257 The transgenic mice with breast cancer were divided into PBS and cRGD-MNPs
258 groups (age 8 weeks, $n = 3$ per group). Two hours post-intravenous injection, the tumour
259 tissue was removed and subjected to Fontana–Masson staining. The slides were
260 immersed in the Fontana–Masson solution, placed in the dark at 4°C for 12–18 h, and
261 then rinsed with distilled water. Next, the slides was put into VG staining solution and
262 stained for 1 minute. Finally, the slides were washed, sealed with neutral balsam and
263 observed under the microscope.

264 **PAI-guided breast cancer surgery on MDA-MB-231 xenograft mice**

265 For surgical resection, cRGD-MNPs ($100\ \mu\text{M}$, $200\ \mu\text{L}$) were intravenously injected
266 into MDA-MB-231 tumour-bearing mice via the tail vein. Each mouse was anaesthetised
267 and placed on a mouse table for position adjustment. The mice remained anaesthetised
268 during the entire imaging acquisition process. Tumour profiles were detected using 3D
269 PA/US imaging two hours after nanoprobe injection. For simulated tumour surgery
270 resection, the surgery procedure was performed in four steps: PAI-guided tumour
271 detection, partial tumour resection (P1–3), PAI detection of the residual tumour, and re-
272 resection of the tumour bed (P4). PA images were acquired both before and after each
273 sequential removal of tumour. Each resection was about a 5–6 mm long and 2–3 mm
274 wide piece of tissue. After each resection, we irrigate the surgical area with saline to
275 resolve the bleeding issues. Surgically excised tissue was stained with haematoxylin
276 and eosin (H&E), according to the standard protocol. To detect the depth of PAI,
277 tumours covering chicken breast with various thickness (1, 2, 3, 5, 7 mm) were
278 performed PAI using the PAI system.

279 **cRGD-MNPs biosafety evaluation**

280 BALB/c mice (4–6 weeks, approximately 20 g) were randomly divided into four
281 groups: control, 1-d cRGD-MNPs, 7-d cRGD-MNPs, and 30-d cRGD-MNPs ($n = 5$ per

282 group). The mice were intravenously injected with saline (control) or cRGD-MNPs
283 (100 μ M, 200 μ L). Body weight was monitored throughout the experiment. Blood
284 samples and major organs (heart, liver, spleen, lung and kidney) were collected after 1
285 (1-d group), 7 (7-d group) or 30 days (control and 30-d groups) post-injection. The
286 blood samples were analysed for serum biochemistry parameters. These parameters
287 included aspartate aminotransferase (AST), alanine aminotransferase (ALT), blood
288 urea nitrogen (BUN) and creatinine (CR). H&E staining was performed on sections of
289 the major organs for histological analysis.

290 **Statistical analysis**

291 Statistical analysis was performed using GraphPad Prism 7.0 (GraphPad Software,
292 CA). The two-tailed paired t-test was used to compare the changes in photoacoustic
293 signals. Data are presented as the mean \pm standard error of the mean. Significant
294 differences between or among the groups are indicated as follows: ns for no significant
295 difference, * for $P < 0.05$, ** for $P < 0.01$, and *** for $P < 0.001$.

296

297 **Results**

298 **Synthesis and characterisation of cRGD-MNPs**

299 The water-soluble MNPs were approximately 4 nm in size based on transmission
300 electron microscopy (Fig. 1a). Polyethylene glycol (PEG) chains were introduced into
301 the MNPs for further biomodification, which was confirmed by ¹H NMR spectra (Fig.
302 S1a). This can reduce the liver accumulation because of the enhanced water solubility.
303 Lastly, the PEG-MNPs were further modified with cyclic Arg-Gly-Asp-d-Phe-Cys
304 [c(RGDfC)] peptide (cRGD), which targets tumour $\alpha_v\beta_3$ integrin [21]. The diameter of
305 the RGD-functionalized PEG-MNPs (cRGD-MNPs) increased to about 9 nm (Fig. 1a).
306 With the modifications of PEG and RGD (i.e., cRGD-MNPs), the surface potential of
307 the MNPs increased from -48 to -8.6 mV (Fig. 1b). MNPs have strong and broad optical
308 absorbance and PA spectra in the wavelength range of visible light to the near-infrared
309 region. The similar absorption and PA spectra between cRGD-MNPs and MNPs
310 indicated that the biomodifications did not influence the absorption properties and
311 intrinsic PA properties of melanin (Fig. 1c, d). Moreover, both the cRGD-MNPs and
312 MNPs showed a linear relationship between concentration and absorbance intensity (R^2
313 =1 and 0.9999 for MNPs and cRGD-MNPs, respectively) (Fig. S1b, c, d) and PA
314 intensity ($R^2 = 0.9637$ and 0.9513 for MNPs and cRGD-MNPs, respectively) (Fig. S1e,
315 f, Fig. 1e) at 680 nm. In addition, the cRGD-MNPs exhibited excellent stability, with
316 no attenuation of the PA signal intensity after storage for a week at 4°C (Fig. 1f).

317 **Targeting ability and cytotoxicity of cRGD-MNPs *in vitro***

318 As seen from the overlay images and quantitative results, the PA signal intensity of
319 MDA-MB-231 cells increased with incubation time from 1 h to 8 h (Fig. 2a). The cells
320 produced significant PA signal intensities after incubation for 4 h, and there was no
321 statistical difference between the 4 h and 8 h time points. As the concentration of cRGD-
322 MNPs increased, the uptake of the probe by the MDA-MB-231 cells also increased (Fig.
323 2b). The concentration of 0.5 μ M was selected for subsequent experiments because
324 there was no statistical difference between 0.5 μ M and 1 μ M in PA signal intensity.

325 Compared to the same concentrations of MNPs and PEG-MNPs, MDA-MB-231 cells
326 incubated with RGD-MNPs showed stronger PA signal intensity (Fig. 2c), which
327 confirmed that more cRGD-MNPs could be internalised by MDA-MB-231 cells.

328 To prove the ability of the cRGD-MNPs to target the integrin $\alpha_v\beta_3$ receptor, we
329 determined their binding affinity using MDA-MB-231 and MCF-10A (a non-neoplastic
330 breast cell line with low expression of $\alpha_v\beta_3$) [22] cells. The PA intensity was markedly
331 enhanced for the MDA-MB-231 cells compared to that of the MCF-10A cells after a 4-
332 h incubation (Fig. 2d). Additionally, when the cells were co-incubated with excess free
333 RGD molecules, the PA signal intensity of the MDA-MB-231 cells became weaker.
334 These data indicated that indeed RGD enhanced the internalisation of the nanoparticles
335 by cancer cells overexpressing the integrin $\alpha_v\beta_3$ receptor. Similarly, strong red
336 fluorescence was observed in MDA-MB-231 cells incubated with Rho-cRGD-MNPs,
337 while MCF-10A cells showed very weak red fluorescence under the same conditions.
338 This phenomenon could be blocked by excessive unlabelled RGD peptide (Fig. 2e).

339 Finally, analysis of cell viability suggested low cytotoxicity for the MNPs, even at a
340 high concentration up to 10 μ M (Fig. 2f).

341 ***In vivo* cRGD-MNPs tumour uptake and the biodistribution of fluorescence-** 342 **labelled cRGD-MNPs**

343 Based on the PAI performance of the cRGD-MNPs *in vitro*, we performed tumour
344 PAI *in vivo*. The *in vivo* PA signal intensity at the tumour site of MDA-MB-231 tumour-
345 bearing mice at various concentration of cRGD-MNPs (50, 100, and 200 μ M) increased
346 gradually and reached a peak two hours post-injection (Fig. S2a). Moreover, the 100
347 μ M and 200 μ M groups exhibited similar PA intensities, which were higher than that
348 observed for the 50 μ M group 2 h post-injection. The tumour targeting capability of the
349 cRGD-MNPs in living mice was further investigated by intravenous injection cRGD-
350 MNPs into tumour-bearing mice using MNPs as a control) (Fig. 3a, b). We showed that
351 tumour sites exhibited a higher PA signal 1 to 2 h after intravenous administration of
352 cRGD-MNPs than MNPs *in vivo*. Moreover, the cRGD-MNPs group had a significantly
353 higher signal-to-background ratio (tumour versus surrounding normal tissue) than the

354 MNPs group two hours post-injection (3.2 ± 0.1 versus 1.7 ± 0.3 , $P < 0.05$) (Fig. 3c).

355 In addition, the PA signal increased approximately 2.1-fold two hours post-injection
356 compared to pre-injection (Fig. S2b). These results indicated that cRGD-MNPs
357 accumulated more in tumours than normal tissue and provided clearer tumour contrast.

358 We also used fluorescence imaging to track the biodistribution of Rho-cRGD-MNPs
359 and Rho-MNPs two hours post-injection (Fig. 3d). The *ex vivo* fluorescence images and
360 intensities of the major organs and tumours suggested more effective accumulation of
361 Rho-cRGD-MNPs into tumour tissue than Rho-MNPs (Fig. 3d, e).

362 ***In vivo* cRGD-MNPs PAI in MMTV-PyVT transgenic mice**

363 To evaluate the PAI performance of cRGD-MNPs, we used the FVB/N-Tg(MMTV-
364 PyVT)634Mul/J spontaneous breast cancer model that closely recapitulate human
365 disease [23]. The transgenic mice underwent PAI before or two hours post-injection
366 (Fig. 4a). Compared to the imaging signal before administration, the PA signal
367 intensities of the mammary glands containing tumour increased 2.5 ± 0.3 -fold (Fig.
368 4b). In contrast, the PA signal intensities of the normal mammary glands did not
369 increase post-injection (0.9 ± 0.1 -fold, Fig. 4b). The pathological status of the
370 mammary glands was confirmed by H&E staining (Fig. 4c). Furthermore, melanin
371 staining confirmed the presence of the MNPs in the tumour tissue after injection of the
372 probe (Fig. 4d). These results indicate that cRGD-MNPs provide a high signal intensity
373 at the tumour site and could distinguish between normal mammary glands and breast
374 tumours.

375 In order to further assess the feasibility of using the cRGD-MNPs to detect a tumour,
376 segmented tumour PAI was performed in MMTV-PyVT transgenic mice with breast
377 cancer (Fig. 4e). The fourth and fifth mammary glands of the transgenic mice were
378 divided into four segments (P1–4), and PA imaging showed complete and intense
379 enhancement of each part of the tumour. *Ex vivo* tissues were imaged using the PAI
380 system, and the tissue signal distribution was consistent with that observed *in vivo* and
381 correlated with the pathological examination (Fig. S3a). The PA images demonstrated

382 an improved contrast profile for breast cancer detection with the cRGD-MNPs.

383 **PAI-guided resection of breast cancer using cRGD-MNPs**

384 We evaluated cRGD-MNPs-based PAI for tumour detection, delineation, and
385 imaging-guided resection. First, the tumours of MDA-MB-231 tumour-bearing mice
386 were examined by PAI preoperatively. The reconstructed three-dimensional (3D) image
387 was used to show the spatial distribution of the cRGD-MNPs at the tumour site, which
388 provided the general profile of a tumour for the development of a surgical plan (Fig.
389 5a). From the PA signals of the cRGD-MNPs, the size and position of the MDA-MB-
390 231-tumour could be defined.

391 Next, we investigated whether the nanoprobe could guide intraoperative tumour
392 resection. In this experiment, MDA-MB-231 tumour-bearing mice underwent
393 consecutive tumour resections two hours post-injection of cRGD-MNPs. Ultrasound
394 (US) images depicted representative subcutaneous transplanted tumours (Fig. 5b). A
395 strong PA signal showed the tumour location before the resection. We then performed
396 partial resection under PAI guidance. The resected tissues for each step are shown in
397 Figure 5b (P1-4). After removal of most of the tumour, the remaining tumour (about 2
398 mm wide) was still visible by PAI. Finally, the remaining tumour was resected until no
399 obvious PA signal was detected. For comparison, tissues with negative PA signals on
400 the tumour bed (P4) were excised again for subsequent pathology examination. The *ex*
401 *vivo* tissue PA signal distribution was consistent with that obtained *in vivo* (Fig. S3b).
402 Pathological examination showed that the tumour had been completely removed, and
403 the tissue with a negative PA signal on the tumour bed was muscle tissue (Fig. 5c). To
404 detect the depth of PAI, we covered the tumours with chicken breasts of various
405 thicknesses and found that the maximum imaging depth was up to 5 mm (Fig. 5d).
406 Taken together, PAI can effectively detect tumours, identify residual masses, and guide
407 surgical resection.

408 ***In vivo* cRGD-MNPs biosafety**

409 The *in vivo* biocompatibility was further evaluated in mice for prolonged durations

410 (1, 7 or 30 days) after intravenous administration of cRGD-MNPs. Saline served as a
411 negative control. No considerable body weight loss was observed for the cRGD-MNPs
412 and control groups over 30 days, indicating that cRGD-MNPs had no significant side
413 effects in mice (Fig. 6a). The serum biochemistry analysis, which included liver
414 function (ALT, AST) and kidney function (BUN, CR) markers, showed negligible
415 variations between the different groups, indicating no detectable toxicity shortly after
416 or a relatively long time after exposure (Fig. 6b). Although cRGD-MNPs also
417 accumulated in the liver and kidneys, negligible liver and kidney damage was induced.
418 H&E staining of the major organs (heart, liver, spleen, lung and kidney) at different
419 times after intravenous injection showed no significant acute or chronic physiological
420 toxicity compared to the control group, indicating the high histocompatibility of the
421 cRGD-MNPs (Fig. 6c). These results indicate that the cRGD-MNPs have high *in vivo*
422 biocompatibility.

423 **Discussion**

424 It remains a significant challenge in BCS to acquire clean margins during primary
425 surgery due to the lack of precision in localising tumours and the inaccuracy of tumour
426 excision by visual inspection and tactile feedback. Imaging-guided surgery is gaining
427 increasing importance in the operating room. It can help detect microscopic tumours or
428 residual lesions that are readily missed during surgery and guide intraoperative surgical
429 margin assessment [24]. Thus, this approach could potentially improve patient outcome
430 following oncologic surgery. In the present study, we demonstrated for the first time
431 that the use of cRGD-MNPs as a targeted PA contrast has the potential to locate
432 tumours and offer a 3D reconstruction of the breast cancer for surgical planning.
433 Although the utility of cRGD-MNPs-mediated PAI or photothermal therapy has been
434 previously demonstrated in animals [17], our study further translates these findings to
435 imaging-guided cancer surgery, showing the feasibility of cRGD-MNPs PAI for
436 consecutive imaging-guided resections of the remaining margins of breast cancer.

437 Melanin is a naturally occurring biopolymer present in many organisms, particularly
438 in the skin and hair. It has a good intrinsic photoacoustic property. By mimicking natural
439 melanin, recent studies have demonstrated that melanin-based nanoparticles could
440 serve as a multimodality nanoplatform for molecular imaging [16, 25, 26]. As in the
441 report of Fan et al [20], we prepared artificial ultras-small MNPs and modified them by
442 conjugating them with c(RGDfC) peptides. cRGD-MNPs have a high affinity for
443 integrin $\alpha_v\beta_3$, which is expressed predominantly on neovascular endothelial cells and
444 tumour cells, including breast cancer cells [27, 28]. Consistent with previous findings,
445 our results demonstrated a higher tumour-targeting capability of cRGD-MNPs
446 compared to MNPs using MDA-MB-231 tumour-bearing mice, indicating that cRGD-
447 MNPs could more specifically target breast cancer xenografts, possibly via the binding
448 to integrin $\alpha_v\beta_3$. Moreover, mammary glands of FVB/N-Tg(MMTV-PyVT)634Mul/J
449 transgenic mice containing carcinoma showed excellent PA intensity enhancement after
450 the administration of cRGD-MNPs compared to the normal mammary gland tissue.
451 These data further indicated that cRGD-MNPs could conveniently serve as a good
452 contrast for breast cancer-specific PAI.

453 MNPs have been used in diverse biomedical applications, such as imaging,
454 controlled drug release, bioengineering and bioelectronics, antioxidant applications and
455 theranostics [29]. Based on the dramatic *in vivo* PAI properties of the cRGD-MNPs in
456 this study, we used these MNPs for PAI-guided surgical navigation. To simulate PAI-
457 guided consecutive resections in a small animal model, we sequentially removed breast
458 tumour tissue using the real-time guidance of PAI, which was validated by subsequent
459 histological analysis. In addition, we found that the tumour, when artificially located in
460 deep tissue, could be clearly imaged and discriminated with a depth of up to 5 mm. A
461 previous study reported the application of PAI with endogenous melanin as contrast for
462 the resection of B16 melanoma liver metastasis [30]. Hepatic melanoma *in vivo* as small
463 as 400 μm could be detected at a depth of up to 7 mm and precisely resected using PAI
464 guidance, demonstrating the advantages of PA (i.e., high resolution, high sensitivity,
465 deep penetration and early detection of hepatic micrometastasis). In a clinical study,
466 PAI-guided pathological evaluation improved the detection rate of metastases
467 compared to the standard protocol in excising sentinel lymph nodes in patients with
468 melanoma (22.9% versus 14.2%) [19]. Taken together with the results of the present
469 study, PAI using melanin or melanin-based nanoparticles could offer a rapid and
470 effective tool for non-invasive detection of small tumour disease of a certain depth.

471 In addition to melanin nanoparticles, several exogenous contrast agents have been
472 used for photoacoustic surgical navigation in animals, including gold nanoparticles [31,
473 32], superparamagnetic iron oxide [33], dye-based agents [34, 35], and carbon-based
474 nanomaterials [36]. All these agents could generate non-invasive PA contrast
475 enhancement when stimulated by laser irradiation at specific wavelengths. However,
476 clinical translation of these agents is prohibitive because of biosafety issues, poor
477 biodegradability, low photostability and unclear biocompatibility [37, 38]. In the
478 present study, the biocompatibility and biosafety of cRGD-MNPs were systematically
479 evaluated both *in vitro* and *in vivo*. As reported previously, the strengths of melanin-
480 like nanomaterials include good biocompatibility and long-term photostability [39, 40],
481 prompting us to explore their biomedical applications, particularly for *in vivo* imaging.
482 Our findings demonstrated that cRGD-MNPs represent a promising contrast agent for

483 further clinical translation.

484 However, this study has a few limitations. First, only PAI alone was applied to
485 surgical navigation. As a previous study reported [20], MNPs are an active platform to
486 simplify the assembling of different imaging moieties, such as positron emission
487 tomography and magnetic resonance imaging. Thus, complementary use of
488 multimodality imaging is promising not only for accurate tumour imaging but also for
489 guiding tumour resection. Further research efforts should be devoted to precise, targeted
490 tumour multimodality imaging. Second, the current methodology using MNPs as a
491 contrast agent is unsuitable for deep-tissue imaging in the human body. Therefore,
492 further improvements of the imaging agents are needed to increase the imaging depth.

493 In this report, we demonstrated the feasibility of PA augmented by the systemic
494 delivery of cRGD-MNPs to detect tumours for preoperative 2D or 3D imaging and
495 guide initial and subsequent resections of breast cancer xenografts. With further
496 development and optimisation, PAI using cRGD-MNPs is expected to be evaluated in
497 breast cancer patients for surgical navigation in the near future.

498

- 500 1. DeSantis C E, Ma J, Gaudet M M, Newman L A, Miller K D, Goding Sauer A, et al. Breast cancer statistics,
501 2019. *CA: a cancer journal for clinicians*. 2019; 69:438-451. DOI: 10.3322/caac.21583.
- 502 2. Darby S, McGale P, Correa C, Taylor C, Arriagada R, Clarke M, et al. Effect of radiotherapy after breast-
503 conserving surgery on 10-year recurrence and 15-year breast cancer death: meta-analysis of individual
504 patient data for 10,801 women in 17 randomised trials. *Lancet*. 2011; 378:1707-1716. DOI:
505 10.1016/S0140-6736(11)61629-2.
- 506 3. Pleijhuis R G, Graafland M, de Vries J, Bart J, de Jong J Svan Dam G M. Obtaining adequate surgical
507 margins in breast-conserving therapy for patients with early-stage breast cancer: current modalities and
508 future directions. *Annals of surgical oncology*. 2009; 16:2717-2730. DOI: 10.1245/s10434-009-0609-z.
- 509 4. Esbona K, Li ZWilke L G. Intraoperative imprint cytology and frozen section pathology for margin
510 assessment in breast conservation surgery: a systematic review. *Annals of surgical oncology*. 2012;
511 19:3236-3245. DOI: 10.1245/s10434-012-2492-2.
- 512 5. Pradipta A R, Tanei T, Morimoto K, Shimazu K, Noguchi S Tanaka K. Emerging Technologies for Real-
513 Time Intraoperative Margin Assessment in Future Breast-Conserving Surgery. *Advanced science*. 2020;
514 7:1901519. DOI: 10.1002/advs.201901519.
- 515 6. Langhans L, Tvedskov T F, Klausen T L, Jensen M-B, Talman M-L, Vejborg I, et al. Radioactive Seed
516 Localization or Wire-guided Localization of Nonpalpable Invasive and In Situ Breast Cancer: A
517 Randomized, Multicenter, Open-label Trial. *Annals of surgery*. 2017; 266:29-35. DOI:
518 10.1097/SLA.0000000000002101.
- 519 7. Ahmed MDouek M. Intra-operative ultrasound versus wire-guided localization in the surgical
520 management of non-palpable breast cancers: systematic review and meta-analysis. *Breast cancer research
521 and treatment*. 2013; 140:435-446. DOI: 10.1007/s10549-013-2639-2.
- 522 8. Qiu S-Q, Dorrius M D, de Jongh S J, Jansen L, de Vries J, Schröder C P, et al. Micro-computed tomography
523 (micro-CT) for intraoperative surgical margin assessment of breast cancer: A feasibility study in breast
524 conserving surgery. *European journal of surgical oncology*. 2018; 44:1708-1713. DOI:
525 10.1016/j.ejso.2018.06.022.
- 526 9. Hernot S, van Manen L, Debie P, Mieog J S DVahrmeijer A L. Latest developments in molecular tracers
527 for fluorescence image-guided cancer surgery. *The Lancet. Oncology*. 2019; 20:e354-e367. DOI:
528 10.1016/S1470-2045(19)30317-1.
- 529 10. Nguyen Q TTsien R Y. Fluorescence-guided surgery with live molecular navigation--a new cutting edge.
530 *Nature reviews. Cancer*. 2013; 13:653-662. DOI: 10.1038/nrc3566.
- 531 11. Wang L VYao J. A practical guide to photoacoustic tomography in the life sciences. *Nature Methods*. 2016;
532 13:627-38. DOI: 10.1038/nmeth.3925.
- 533 12. Li R, Lan L, Xia Y, Wang P, Han L K, Dunnington G L, et al. High-speed Intraoperative Assessment of
534 Breast Tumor Margins by Multimodal Ultrasound and Photoacoustic Tomography. *Med Devices Sens*.
535 2018; 1. DOI: 10.1002/mds3.10018.
- 536 13. Wong T T W, Zhang R, Hai P, Zhang C, Pleitez M A, Aft R L, et al. Fast label-free multilayered histology-
537 like imaging of human breast cancer by photoacoustic microscopy. *Science advances*. 2017; 3:e1602168.
538 DOI: 10.1126/sciadv.1602168.
- 539 14. Li R, Wang P, Lan L, Lloyd F P, Goergen C J, Chen S, et al. Assessing breast tumor margin by multispectral
540 photoacoustic tomography. *Biomedical optics express*. 2015; 6:1273-1281. DOI: 10.1364/BOE.6.001273.
- 541 15. Weber J, Beard P CBohndiek S E. Contrast agents for molecular photoacoustic imaging. *Nature Methods*.
542 2016; 13:639-50. DOI: 10.1038/nmeth.3929.

- 543 16. Park J, Moon HHong S. Recent advances in melanin-like nanomaterials in biomedical applications: a mini
544 review. *Biomaterials research*. 2019; 23:24-24. DOI: 10.1186/s40824-019-0175-9.
- 545 17. Caldas M, Santos A C, Veiga F, Rebelo R, Reis R LCorrelo V M. Melanin nanoparticles as a promising
546 tool for biomedical applications - a review. *Acta Biomaterialia*. 2020; 105:26-43. DOI:
547 10.1016/j.actbio.2020.01.044.
- 548 18. Fu Q, Zhu R, Song J, Yang HChen X. Photoacoustic Imaging: Contrast Agents and Their Biomedical
549 Applications. *Advanced materials (Deerfield Beach, Fla.)*. 2019; 31:e1805875. DOI:
550 10.1002/adma.201805875.
- 551 19. Stoffels I, Morscher S, Helfrich I, Hillen U, Leyh J, Lehy J, et al. Metastatic status of sentinel lymph nodes
552 in melanoma determined noninvasively with multispectral optoacoustic imaging. *Science translational
553 medicine*. 2015; 7:317ra199. DOI: 10.1126/scitranslmed.aad1278.
- 554 20. Fan Q, Cheng K, Hu X, Ma X, Zhang R, Yang M, et al. Transferring biomarker into molecular probe:
555 melanin nanoparticle as a naturally active platform for multimodality imaging. *Journal of the American
556 Chemical Society*. 2014; 136:15185-94. DOI: 10.1021/ja505412p.
- 557 21. Nieberler M, Reuning U, Reichart F, Notni J, Wester H J, Schwaiger M, et al. Exploring the Role of RGD-
558 Recognizing Integrins in Cancer. *Cancers (Basel)*. 2017; 9. DOI: 10.3390/cancers9090116.
- 559 22. Veneti E, Tu R SAuguste D T. RGD-Targeted Liposome Binding and Uptake on Breast Cancer Cells Is
560 Dependent on Elastin Linker Secondary Structure. *Bioconjugate Chemistry*. 2016; 27:1813-1821. DOI:
561 10.1021/acs.bioconjchem.6b00205.
- 562 23. Shishido S N, Delahaye A, Beck ANguyen T A. The anticancer effect of PQ1 in the MMTV-PyVT mouse
563 model. *International Journal of Cancer*. 2014; 134:1474-1483. DOI: 10.1002/ijc.28461.
- 564 24. Mondal S B, O'Brien C M, Bishop K, Fields R C, Margenthaler J AAchilefu S. Repurposing Molecular
565 Imaging and Sensing for Cancer Image-Guided Surgery. *Journal of nuclear medicine*. 2020; 61:1113-1122.
566 DOI: 10.2967/jnumed.118.220426.
- 567 25. Liu H, Yang Y, Liu Y, Pan J, Wang J, Man F, et al. Melanin-Like Nanomaterials for Advanced Biomedical
568 Applications: A Versatile Platform with Extraordinary Promise. *Advanced science*. 2020; 7:1903129. DOI:
569 10.1002/advs.201903129.
- 570 26. Zhang L, Sheng D, Wang D, Yao Y, Yang K, Wang Z, et al. Bioinspired Multifunctional Melanin-Based
571 Nanoliposome for Photoacoustic/Magnetic Resonance Imaging-Guided Efficient Photothermal Ablation
572 of Cancer. *Theranostics*. 2018; 8:1591-1606. DOI: 10.7150/thno.22430.
- 573 27. Zhang J, Mao F, Niu G, Peng L, Lang L, Li F, et al. Ga-BBN-RGD PET/CT for GRPR and Integrin α
574 Imaging in Patients with Breast Cancer. *Theranostics*. 2018; 8:1121-1130. DOI: 10.7150/thno.22601.
- 575 28. Beer A J, Niemeyer M, Carlsen J, Sarbia M, Nährig J, Watzlowik P, et al. Patterns of alphavbeta3
576 expression in primary and metastatic human breast cancer as shown by 18F-Galacto-RGD PET. *Journal
577 of nuclear medicine*. 2008; 49:255-259. DOI: 10.2967/jnumed.107.045526.
- 578 29. Hong Z-Y, Feng H-YBu L-H. Melanin-based Nanomaterials: The promising Nanoplatforms for Cancer
579 diagnosis and therapy. *Nanomedicine*. 2020:102211. DOI: 10.1016/j.nano.2020.102211.
- 580 30. Yu Q, Huang S, Wu Z, Zheng J, Chen XNie L. Label-free Visualization of Early Cancer Hepatic
581 Micrometastasis and Intraoperative Image-guided Surgery by Photoacoustic Imaging. *Journal of nuclear
582 medicine*. 2019; 61:1079-1085. DOI: 10.2967/jnumed.119.233155.
- 583 31. Kircher M F, de la Zerda A, Jokerst J V, Zavaleta C L, Kempen P J, Mittra E, et al. A brain tumor molecular
584 imaging strategy using a new triple-modality MRI-photoacoustic-Raman nanoparticle. *Nature medicine*.
585 2012; 18:829-834. DOI: 10.1038/nm.2721.
- 586 32. Guan T, Shang W, Li H, Yang X, Fang C, Tian J, et al. From Detection to Resection: Photoacoustic

- 587 Tomography and Surgery Guidance with Indocyanine Green Loaded Gold Nanorod@liposome Core-Shell
588 Nanoparticles in Liver Cancer. *Bioconjugate chemistry*. 2017; 28:1221-1228. DOI:
589 10.1021/acs.bioconjchem.7b00065.
- 590 33. Thawani J P, Amirshaghghi A, Yan L, Stein J M, Liu J, Tsourkas A. Photoacoustic-Guided Surgery with
591 Indocyanine Green-Coated Superparamagnetic Iron Oxide Nanoparticle Clusters. *Small*. 2017; 13. DOI:
592 10.1002/sml.201701300.
- 593 34. Wilson K E, Bachawal S V, Willmann J K. Intraoperative Resection Guidance with Photoacoustic and
594 Fluorescence Molecular Imaging Using an Anti-B7-H3 Antibody-Indocyanine Green Dual Contrast Agent.
595 *Clinical cancer research : an official journal of the American Association for Cancer Research*. 2018;
596 24:3572-3582. DOI: 10.1158/1078-0432.CCR-18-0417.
- 597 35. Han Z, Shang W, Liang X, Yan H, Hu M, Peng L, et al. An Innovation for Treating Orthotopic Pancreatic
598 Cancer by Preoperative Screening and Imaging-Guided Surgery. *Mol Imaging Biol*. 2019; 21:67-77. DOI:
599 10.1007/s11307-018-1209-8.
- 600 36. De la Zerda A, Zavaleta C, Keren S, Vaithilingam S, Bodapati S, Liu Z, et al. Carbon nanotubes as
601 photoacoustic molecular imaging agents in living mice. *Nature nanotechnology*. 2008; 3:557-62. DOI:
602 10.1038/nnano.2008.231.
- 603 37. Zhang X-D, Wu D, Shen X, Liu P-X, Yang N, Zhao B, et al. Size-dependent in vivo toxicity of PEG-
604 coated gold nanoparticles. *International journal of nanomedicine*. 2011; 6:2071-2081. DOI:
605 10.2147/IJN.S21657.
- 606 38. Bussy C, Methven L, Kostarelos K. Hemotoxicity of carbon nanotubes. *Advanced Drug Delivery Reviews*.
607 2013; 65:2127-2134. DOI: 10.1016/j.addr.2013.10.008.
- 608 39. Liu Y, Ai K, Liu J, Deng M, He Y, Lu L. Dopamine-melanin colloidal nanospheres: an efficient near-
609 infrared photothermal therapeutic agent for in vivo cancer therapy. *Advanced materials*. 2013; 25:1353-
610 1359. DOI: 10.1002/adma.201204683.
- 611 40. Liu X, Cao J, Li H, Li J, Jin Q, Ren K, et al. Mussel-inspired polydopamine: a biocompatible and
612 ultrastable coating for nanoparticles in vivo. *ACS nano*. 2013; 7:9384-9395. DOI: 10.1021/nn404117j.

613

614

615 **Declarations**

616 **Funding**

617 The present study was supported by the National Natural Science Foundation of
618 China (No. 91859120), Natural Science Foundation of Guangdong Province (No.
619 2016A030312008), Scientific Research Fund of Traditional Chinese Medicine Bureau
620 of Guangdong Province (No. 20181146), Start-Up Fund for High-Talents from
621 Xiang'an Hospital of Xiamen University (No. PM201809170013).

622 **Conflict of interest**

623 The authors declare that they have no conflicts of interest.

624 **Data availability**

625 The datasets generated during and/or analysed during the current study are available
626 from the corresponding author on reasonable request.

627 **Contributor Information**

628 Jing-Jing Liu conducted experiments and wrote the manuscript. Zun Wang
629 coordinated and performed the study and drafted the manuscript. Li-Ming Nie directed
630 the experimental methods. Yuan-Yuan Zhu, Ge Li and Lin-Ling Lin cultured cells, raised
631 mice and conducted experiments. Min Chen developed the experimental design and
632 directed the study. Guo-Jun Zhang designed and directed the study and finalised the
633 manuscript.

634 **Ethical approval**

635 Approval was obtained from the ethics committee of Xiamen University. The
636 procedures used in this study adhere to the tenets of the Declaration of Helsinki.

637

638 **Figure Legends**

639 **Scheme 1 Workflow of cRGD-MNPs for intraoperative imaging-guided surgery**
640 **by photoacoustic imaging.**

641

642 **Fig. 1 Characterisation of cRGD-MNPs.** **a** Representative transmission electron
643 microscopy images of MNPs (left) and cRGD-MNPs (right), scale bar: 20 nm. **b** Zeta
644 potential of MNPs, PEG-MNPs and cRGD-MNPs in aqueous solution. **c** UV-vis-NIR
645 spectra of MNPs and cRGD-MNPs. **d** PA spectra of MNPs and cRGD-MNPs. **e** The
646 photoacoustic signal produced by MNPs and cRGD-MNPs was linear at concentrations
647 from 3.75 to 120 μM . Upper panel: the original PA image. **f** PA signal intensities of
648 cRGD-MNPs in PBS (pH = 7.4) stored for one week. Data are presented as the mean \pm
649 SD (n = 3).

650

651 **Fig. 2 *In vitro* uptake and cytotoxicity of cRGD-MNPs.** **a** PA images and signal
652 intensities of MDA-MB-231 cells incubated with cRGD-MNPs for various times (0, 1,
653 2, 4 and 8 h). **b** PA images and signal intensities of MDA-MB-231 cells incubated with
654 cRGD-MNPs at various concentrations (0, 0.125, 0.25, 0.5 and 1 μM). **c** PA images and
655 signal intensities of MDA-MB-231 cells incubated with 0.5 μM MNPs, PEG-MNPs or
656 cRGD-MNPs for 4 h. PBS was used as a negative control. **d** PA images and signal
657 intensities of MCF-10A and MDA-MB-231 cells after incubation with cRGD-MNPs
658 for 4 h with or without free RGD blocking. **e** CLSM images of MCF-10A and MDA-
659 MB-231 cells incubated with Rho-cRGD-MNPs for 4 h with or without free RGD
660 blocking. Scale bar: 20 μm . **f** MDA-MB-231 cell viability after incubation with MNPs,
661 PEG-MNPs or cRGD-MNPs at gradient concentrations using standard MTS assay.
662 Data are presented as the mean \pm SD (n =)3, *** $P < 0.001$.

663

664 **Fig. 3 Tumour-targeting and biodistribution of cRGD-MNPs using an MDA-MB-**
665 **231 xenograft mouse model.** **a** *In vivo* merged PA and US images of MDA-MB-231
666 tumour-bearing mice at various times (pre, 1, 2, 4 and 12 h) after intravenous injection

667 of MNPs or cRGD-MNPs (100 μ M, 200 μ L). Scale bar: 2 mm. **b** Quantitative analysis
668 of PA intensities of tumour sites at the different time points in **(a)**. **c** Signal-to-
669 background ratio of the tumour region two hours post-injection of MNPs or cRGD-
670 MNPs. **d** The biodistribution of rhodamine-labelled MNPs or cRGD-MNPs in the heart,
671 liver, spleen, lung, kidney and tumour from MDA-MB-231 tumour-bearing mice two
672 hours post-injection. **e** Quantitative analysis of the fluorescence intensities of the tissues
673 in **(d)**. Data are presented as the mean \pm SD ($n = 3$); *** $P < 0.001$, * $P < 0.05$.

674

675 **Fig. 4 PAI for mammary glands containing spontaneous breast cancer in MMTV-
676 PyVT transgenic mice. a** Representative US and PA images of cRGD-MNPs
677 accumulation in mice with normal mammary glands or breast cancer. Scale bar: 2 mm.
678 **b** PA signal intensities of breast tumours and normal mammary glands in transgenic
679 mice two hours after tail-vein injection of cRGD-MNPs compared to 0 h. **c**
680 Histopathological examination of the tissues from **(a)**. Scale bar: 2 mm. **d** Fontana-
681 Masson staining of *ex vivo* tumour tissue. Black particles representing the MNPs were
682 not observed in the non-injected nanoprobe group (left). Black particles representing
683 the cRGD-MNPs were observed in the injection probe group (right). The image in the
684 lower right corner (black square) is an enlarged image of the upper left corner area.
685 Scale bar: 200 μ m. **e** US (top), PA (middle) and histological (bottom) images of the 4th
686 and 5th pairs of mammary glands in an 8-week-old MMTV-PyVT mouse. The enlarged
687 mammary glands and different regional tissue (P1-4) are outlined with dotted orange
688 and green lines, respectively. The dotted blue line outlines the tissue inferior to the
689 mammary gland. Scale bar: 2 mm. Data are presented as the mean \pm SD ($n = 3$); * $P <$
690 0.05.

691

692 **Fig. 5 PAI-guided tumour resection in MDA-MB-231 tumour-bearing mice. a**
693 Render, axial, sagittal and coronal images showing the tumour distribution. Scale bar:
694 2 mm. **b** Anatomical US (top) and PA (bottom) images showing the tumour region
695 (dotted orange line) in MDA-MB-231 tumour-bearing mice *in vivo*. The tissue portion
696 to be resected (P1-4) is highlighted with a green dashed circle. Scale bar: 2 mm. **c**

697 Histological images (top) of resected tissue pieces. Scale bar: 2 mm. Enlarged images
698 of regions marked with black boxes are also shown (bottom). Scale bar: 100 μm . **d** PA
699 and US images of tumour tissues covered by different thicknesses of chicken breast
700 under 680 nm laser excitation *in vitro*. Scale bar: 2 mm.

701

702 **Fig. 6 The biosafety of cRGD-MNPs.** **a** Body weight curves for mice treated
703 intravenously with saline (control) or cRGD-MNPs. **b** Serum biochemistry results
704 (liver function and renal function) for BALB/c mice at various time points (1, 7 and 30
705 days) after intravenous injection of cRGD-MNPs or saline (controls). The units of ALT
706 and AST are U/L; the units of BUN and CR are mmol/L and $\mu\text{mol/L}$, respectively. **c**
707 H&E staining of vital organs (heart, liver, spleen, lung and kidney) from each group.
708 Scale bar: 200 μm . Data are presented as the mean \pm SD (n = 5).

Figures

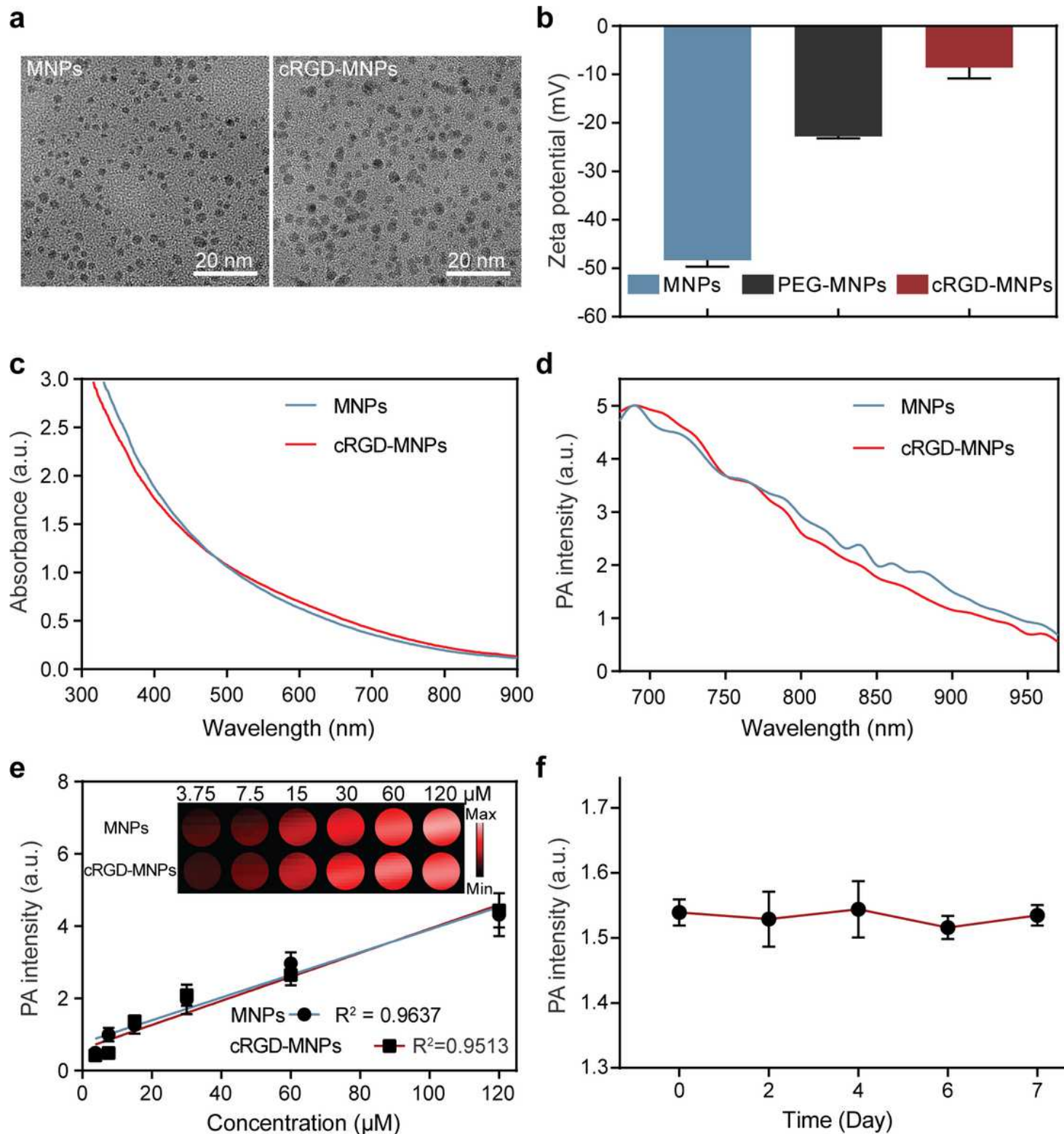


Figure 1

Characterisation of cRGD-MNPs. a Representative transmission electron microscopy images of MNPs (left) and cRGD-MNPs (right), scale bar: 20 nm. b Zeta potential of MNPs, PEG-MNPs and cRGD-MNPs in aqueous solution. c UV-vis-NIR spectra of MNPs and cRGD-MNPs. d PA spectra of MNPs and cRGD-

MNPs. e The photoacoustic signal produced by MNPs and cRGD-MNPs was linear at concentrations from 3.75 to 120 μM . Upper panel: the original PA image. f PA signal intensities of cRGD-MNPs in PBS (pH = 7.4) stored for one week. Data are presented as the mean \pm SD (n = 3).

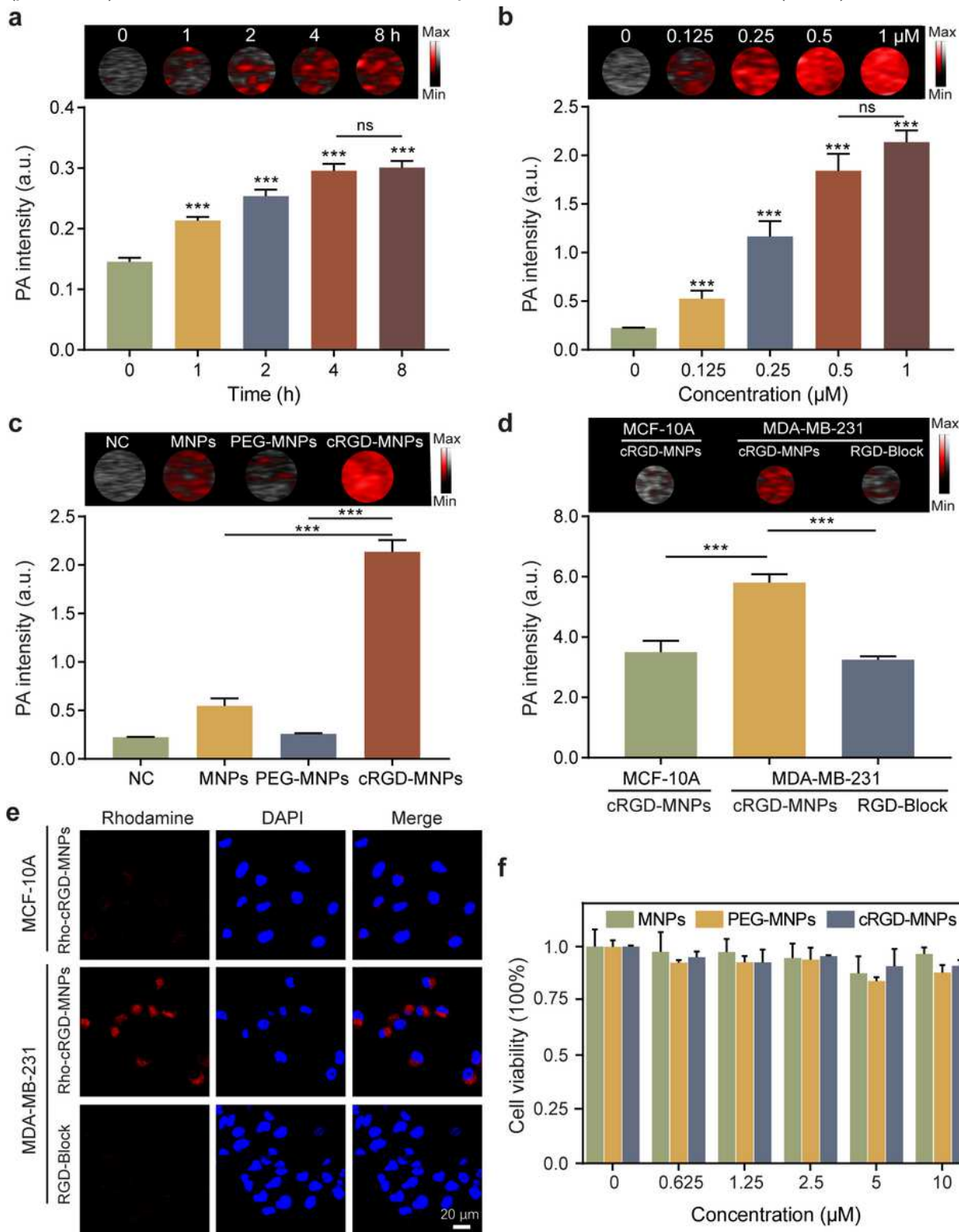


Figure 2

In vitro uptake and cytotoxicity of cRGD-MNPs. a PA images and signal intensities of MDA-MB-231 cells incubated with cRGD-MNPs for various times (0, 1, 2, 4 and 8 h). b PA images and signal intensities of

MDA-MB-231 cells incubated with cRGD-MNPs at various concentrations (0, 0.125, 0.25, 0.5 and 1 μ M). c PA images and signal intensities of MDA-MB-231 cells incubated with 0.5 μ M MNPs, PEG-MNPs or cRGD-MNPs for 4 h. PBS was used as a negative control. d PA images and signal intensities of MCF-10A and MDA-MB-231 cells after incubation with cRGD-MNPs for 4 h with or without free RGD blocking. e CLSM images of MCF-10A and MDA-MB-231 cells incubated with Rho-cRGD-MNPs for 4 h with or without free RGD blocking. Scale bar: 20 μ m. f MDA-MB-231 cell viability after incubation with MNPs, PEG-MNPs or cRGD-MNPs at gradient concentrations using standard MTS assay. Data are presented as the mean \pm SD (n =)3, *** P < 0.001.

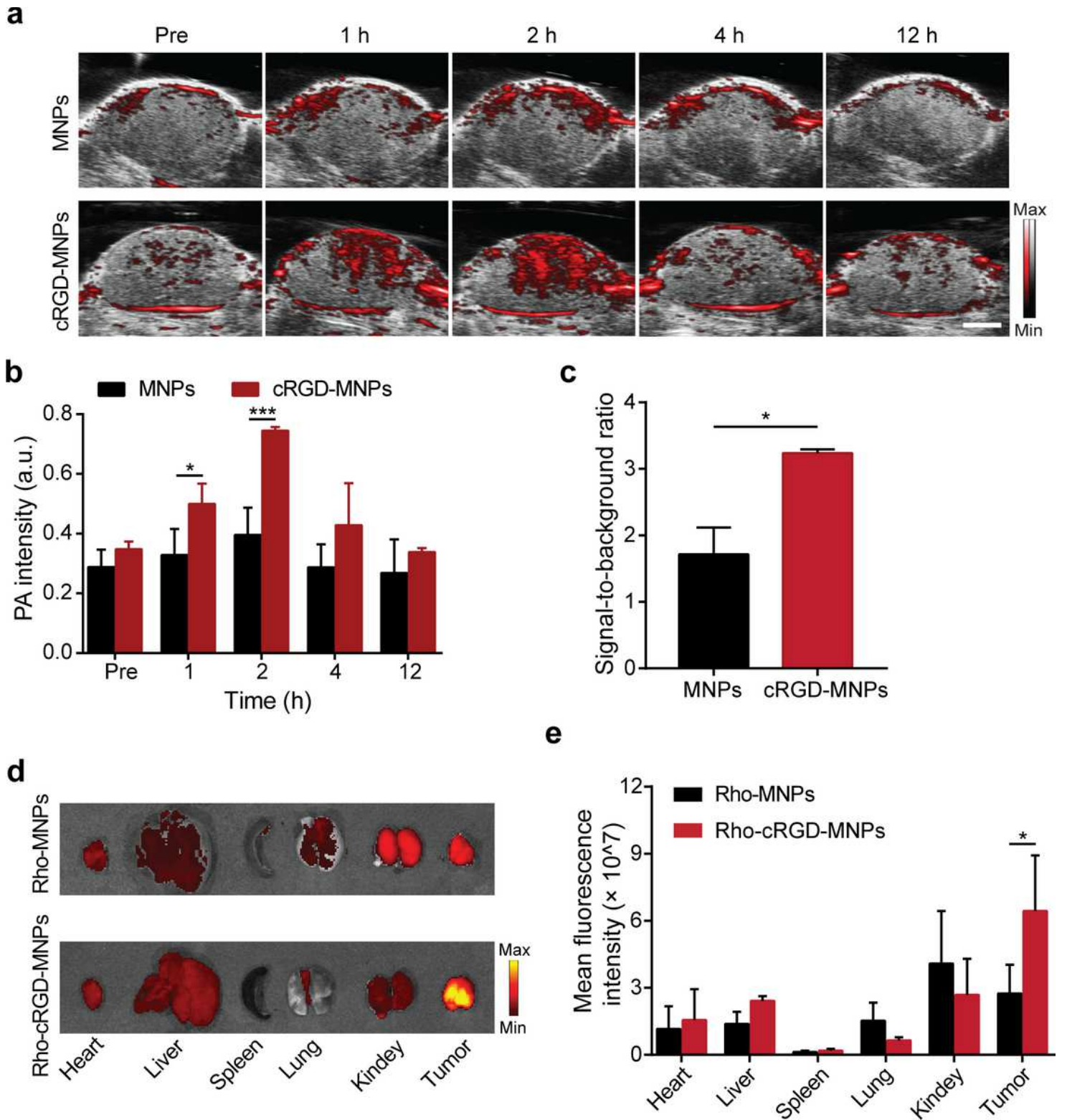


Figure 3

Tumour-targeting and biodistribution of cRGD-MNPs using an MDA-MB-231 xenograft mouse model. **a** In vivo merged PA and US images of MDA-MB-231 tumour-bearing mice at various times (pre, 1, 2, 4 and 12 h) after intravenous injection of MNPs or cRGD-MNPs (100 μ M, 200 μ L). Scale bar: 2 mm. **b** Quantitative analysis of PA intensities of tumour sites at the different time points in (a). **c** Signal-to-background ratio of the tumour region two hours post-injection of MNPs or cRGD-MNPs. **d** The biodistribution of

rhodamine-labelled MNPs or cRGD-MNPs in the heart, liver, spleen, lung, kidney and tumour from MDA-MB-231 tumour-bearing mice two hours post-injection. e Quantitative analysis of the fluorescence intensities of the tissues in (d). Data are presented as the mean \pm SD (n = 3); *** P < 0.001, * P < 0.05.

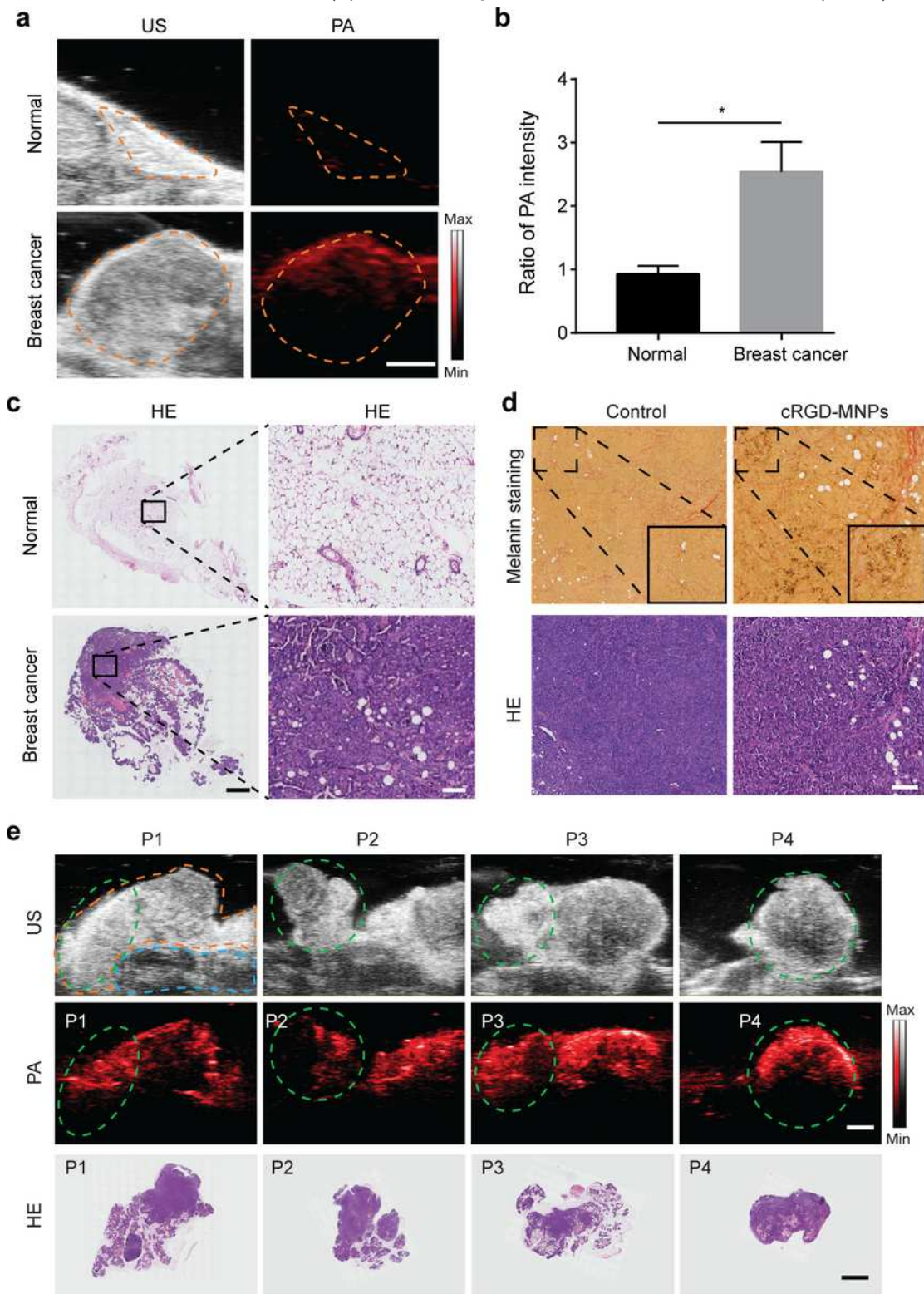


Figure 4

PAI for mammary glands containing spontaneous breast cancer in MMTV-PyVT transgenic mice. a Representative US and PA images of cRGD-MNPs accumulation in mice with normal mammary glands or

breast cancer. Scale bar: 2 mm. b PA signal intensities of breast tumours and normal mammary glands in transgenic mice two hours after tail-vein injection of cRGD-MNPs compared to 0 h. c Histopathological examination of the tissues from (a). Scale bar: 2 mm. d Fontana–Masson staining of ex vivo tumour tissue. Black particles representing the MNPs were not observed in the non-injected nanoprobe group (left). Black particles representing the cRGD-MNPs were observed in the injection probe group (right). The image in the lower right corner (black square) is an enlarged image of the upper left corner area. Scale bar: 200 μ m. e US (top), PA (middle) and histological (bottom) images of the 4th and 5th pairs of mammary glands in an 8-week-old MMTV-PyVT mouse. The enlarged mammary glands and different regional tissue (P1–4) are outlined with dotted orange and green lines, respectively. The dotted blue line outlines the tissue inferior to the mammary gland. Scale bar: 2 mm. Data are presented as the mean \pm SD (n = 3); * P < 0.05.

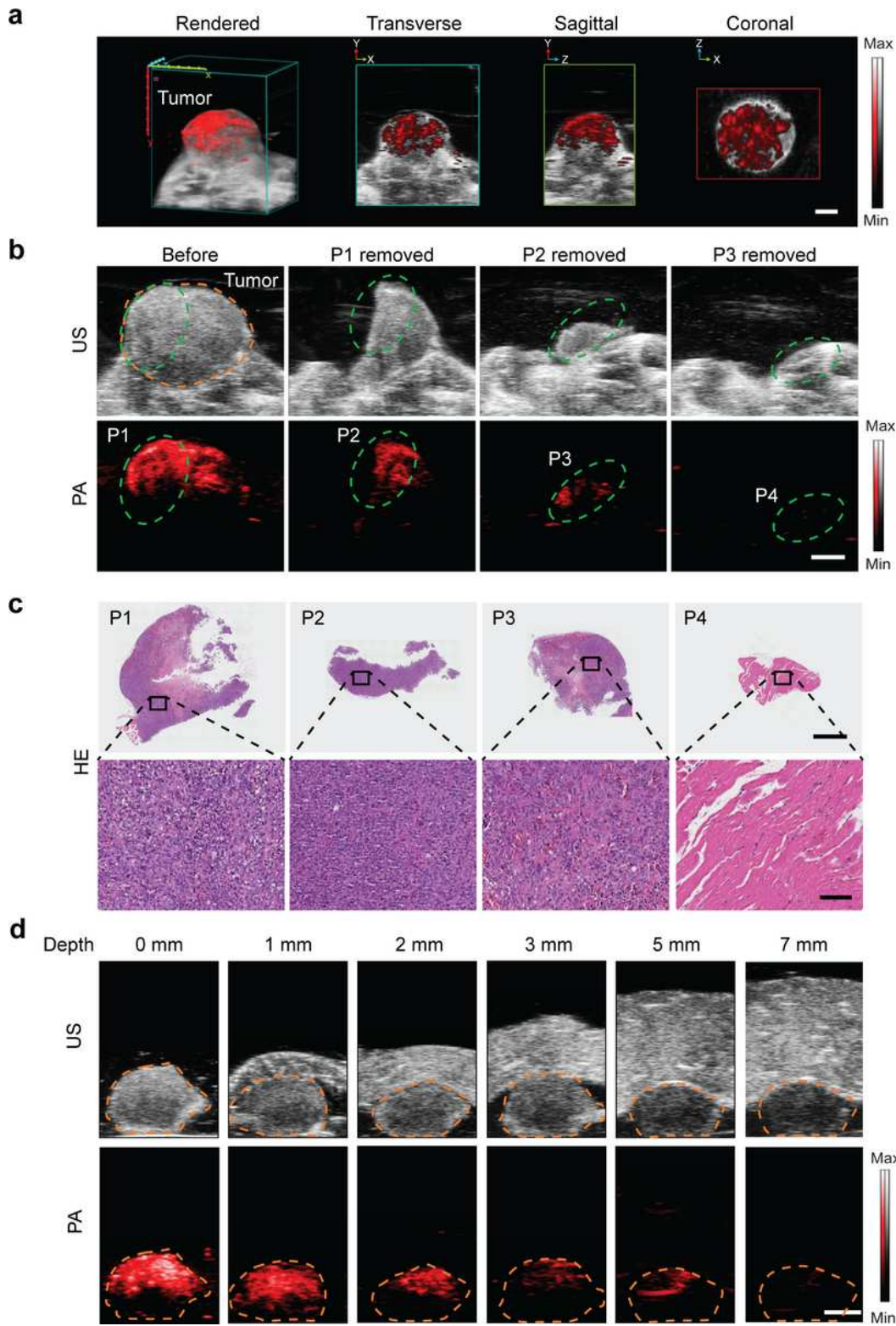


Figure 5

PAI-guided tumour resection in MDA-MB-231 tumour-bearing mice. a Render, axial, sagittal and coronal images showing the tumour distribution. Scale bar: 2 mm. b Anatomical US (top) and PA (bottom) images showing the tumour region (dotted orange line) in MDA-MB-231 tumour-bearing mice in vivo. The tissue portion to be resected (P1-4) is highlighted with a green dashed circle. Scale bar: 2 mm. c Histological images (top) of resected tissue pieces. Scale bar: 2 mm. Enlarged images of regions marked

with black boxes are also shown (bottom). Scale bar: 100 μm . d PA and US images of tumour tissues covered by different thicknesses of chicken breast under 680 nm laser excitation in vitro. Scale bar: 2 mm.

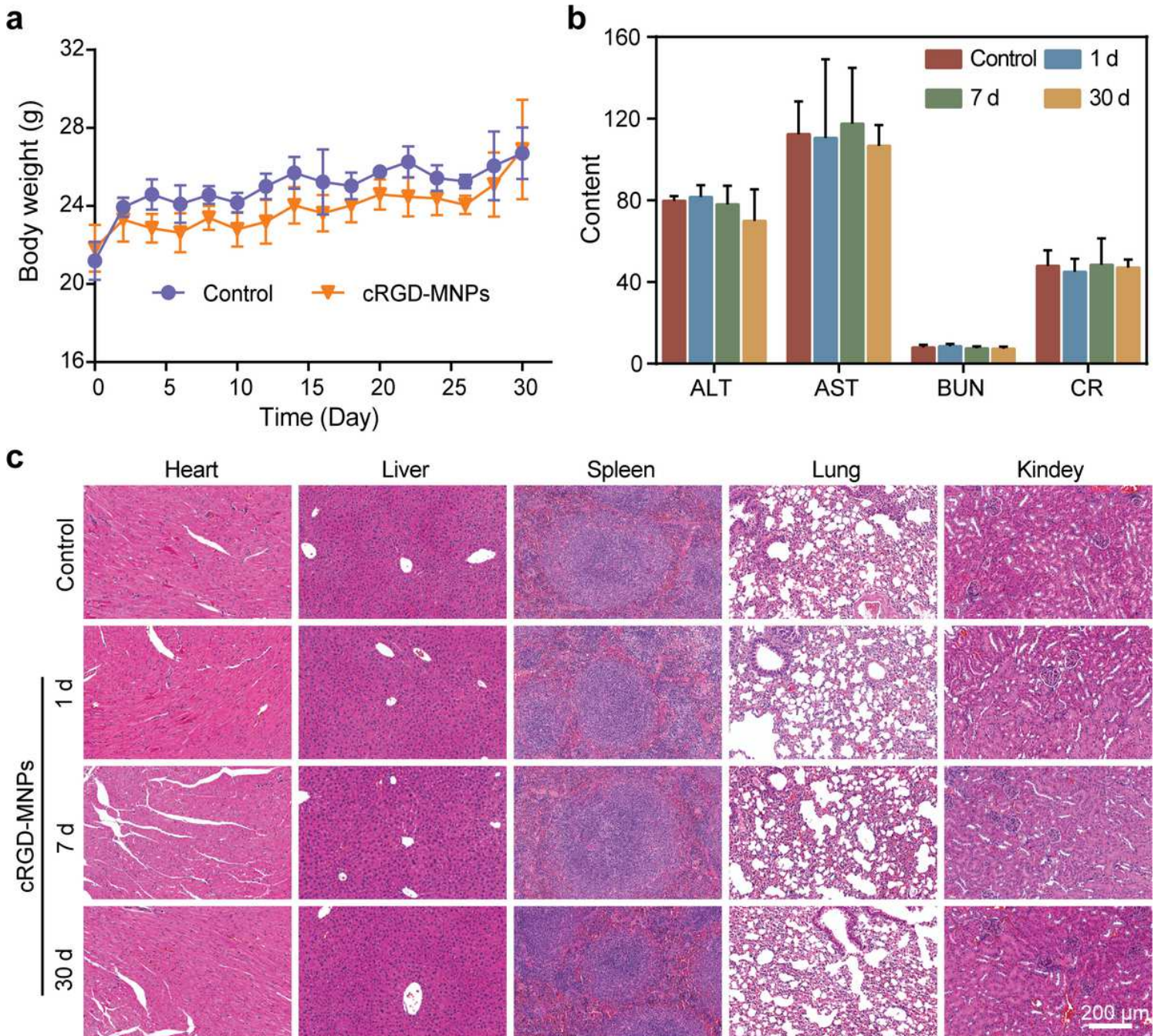


Figure 6

The biosafety of cRGD-MNPs. a Body weight curves for mice treated intravenously with saline (control) or cRGD-MNPs. b Serum biochemistry results (liver function and renal function) for BALB/c mice at various time points (1, 7 and 30 days) after intravenous injection of cRGD-MNPs or saline (controls). The units of ALT and AST are U/L; the units of BUN and CR are mmol/L and $\mu\text{mol/L}$, respectively. c H&E staining of vital organs (heart, liver, spleen, lung and kidney) from each group. Scale bar: 200 μm . Data are presented as the mean \pm SD (n = 5).

Supplementary Files

This is a list of supplementary files associated with this preprint. Click to download.

- [scheme.png](#)
- [SupplementaryInformation.pdf](#)